Total density profile of massive early-type galaxies in H orizon -AGN simulation: impact of AGN feedback and comparison with observations

Sébastien Peirani, Alessandro Sonnenfeld, Raphael Gavazzi, Masamune Oguri, Yohan Dubois, Joe Silk, Christophe Pichon, Julien Devriendt, Sugata Kaviraj

Monthly Notices
of the
ROYAL ASTRONOMICAL SOCIETY

MNRAS **483,** 4615–4627 (2019)
Advance Access publication 2018 December 21

doi:10.1093/mnras/sty3475

Total density profile of massive early-type galaxies in HORIZON-AGN simulation: impact of AGN feedback and comparison with observations

Sébastien Peirani,[1,2,3,4★] Alessandro Sonnenfeld,[3] Raphaël Gavazzi,[2] Masamune Oguri,[3,4,5] Yohan Dubois,[2★] Joe Silk,[2,6,7] Christophe Pichon,[2,8] Julien Devriendt[6,9] and Sugata Kaviraj[10]

[1]*Université Côte d'Azur, Observatoire de la Côte d'Azur, CNRS, Laboratoire Lagrange, Bd de l'Observatoire, CS 34229, F-06304 Nice Cedex 4, France*
[2]*Institut d'Astrophysique de Paris (UMR 7095: CNRS & UPMC), 98 bis Bd Arago, F-75014 Paris, France*
[3]*Kavli IPMU (WPI), UTIAS, The University of Tokyo, Kashiwa, Chiba 277-8583, Japan*
[4]*Department of Physics, The University of Tokyo, 7-3-1 Hongo, Bunkyo-ku, Tokyo 113-0033, Japan*
[5]*Research Center for the Early Universe, School of Science, The University of Tokyo, 7-3-1 Hongo, Bunkyo-ku, Tokyo 113-0033, Japan*
[6]*Sub-department of Astrophysics, University of Oxford, Keble Road, Oxford OX1 3RH, UK*
[7]*Department of Physics and Astronomy, The Johns Hopkins University Homewood Campus, Baltimore, MD 21218, USA*
[8]*Korea Institute of Advanced Studies (KIAS) 85 Hoegiro, Dongdaemun-gu, Seoul, 02455, Republic of Korea*
[9]*Observatoire de Lyon, UMR 5574, 9 avenue Charles André, Saint Genis Laval, F-69561, France*
[10]*Centre for Astrophysics Research, University of Hertfordshire, College Lane, Hatfield, Herts, AL10 9AB, UK*

Accepted 2018 December 18. Received 2018 December 18; in original form 2018 January 22

ABSTRACT

Using the two large cosmological hydrodynamical simulations, HORIZON-AGN ($H_{\rm AGN}$) and HORIZON-NOAGN ($H_{\rm noAGN}$, no AGN feedback), we investigate how a typical sub-grid model for AGN feedback affects the evolution of the total density profiles (dark matter + stars) at the effective radius of massive early-type galaxies ($M_* \geq 10^{11}\,{\rm M}_\odot$). We have studied the dependencies of the mass-weighted density slope $\gamma'_{\rm tot}$ with the effective radius, the galaxy mass and the host halo mass at $z \sim 0.3$ and found that the inclusion of AGN feedback always leads to a much better agreement with observational values and trends. Our analysis also suggests that the inclusion of AGN feedback favours a strong correlation between $\gamma'_{\rm tot}$ and the density slope of the dark matter component while, in the absence of AGN activity, $\gamma'_{\rm tot}$ is rather strongly correlated with the density slope of the stellar component. Finally, we find that $\gamma'_{\rm tot}$ derived from our samples of galaxies increases from $z = 2$ to $z = 0$, in good agreement with the expected observational trend. The derived slopes are slightly lower than in the data when AGN is included because the simulated galaxies tend to be too extended, especially the least massive ones. However, the simulated compact galaxies without AGN feedback have $\gamma'_{\rm tot}$ values that are significantly too high compared to observations.

Key words: methods: numerical – galaxies: evolution – galaxies: haloes – galaxies: jets – dark matter.

1 INTRODUCTION

Despite the early discovery of tight scaling relations between the physical properties of the apparently simple 'red and dead' population of early-type galaxies (ETGs), the origin and evolution of these relations are still poorly understood (White & Rees 1978; Djorgovski & Davis 1987; Dressler et al. 1987; Faber et al. 1987). These properties concern the stellar mass profile, stellar populations, metallicity, halo mass to stellar mass relation, as well as stellar mass to central supermassive black hole (BH) mass (Magorrian et al. 1998; Ferrarese & Merritt 2000; Häring & Rix 2004; Gültekin et al. 2009). In the standard ΛCDM paradigm, progenitors of massive collapsed structures such as massive ETGs form at high redshift by the accretion of cold filamentary gas (Rees & Ostriker 1977; White & Frenk 1991; Birnboim & Dekel 2003; Kereš et al. 2005; Ocvirk, Pichon & Teyssier 2008; Dekel et al. 2009; van de Voort et al. 2011) that must be stopped at low redshift by some feedback mechanism associated with the central active galactic nucleus (AGN) (Silk & Rees 1998; King 2003; Wyithe & Loeb 2003). The emerging picture is that they are formed at a redshift larger than 3 and almost fully assembled by $z \sim 1$ (e.g. Renzini 2006). One important conclusion is that their central regions must be virialized with a self-similar structure as early as $z \sim 1$ (Sheth

★ E-mail: speirani@oca.eu (SP); dubois@iap.fr (YD)

et al. 2003) irrespective of the continuous accretion of dark and luminous matter within the ΛCDM hierarchical merging process. This ETG property may be explained if internal regions (within ∼2 effective radii) behave like a dynamical attractor featuring an invariant phase space density in spite of their accretion history (Loeb & Peebles 2003). The dark matter (DM) and stellar components seem to work together in building a 'universal' nearly isothermal total density profile, even though neither of these components is well approximated by an isothermal profile.

In the past few years, the deep study of ETGs playing the role of strong gravitational lenses has led to major developments in the observational side. Indeed, the strong lensing allows very accurate estimation of the total mass at the Einstein radius of such systems and can therefore be combined with other traditional methods such as stellar velocity dispersion (Miralda-Escude 1995; Natarajan & Kneib 1996; Sand, Treu & Ellis 2002; Treu & Koopmans 2002; Newman et al. 2009), and stellar mass maps from multicolour imaging and/or spectroscopy. Such a combination is expected to break the degeneracies inherent to each method alone such as, for instance, the mass-anisotropy degeneracy, bulge-halo degeneracy and the stellar mass/initial mass function (IMF) degeneracy (e.g. Koopmans & Treu 2003; Treu & Koopmans 2004; Auger et al. 2010; Treu et al. 2010; Dutton et al. 2013). Weak lensing analysis can also provide additional constraints though it is not yet possible to use for individual galaxies (Gavazzi et al. 2007; Jiang & Kochanek 2007; Lagattuta et al. 2010). Another way to break the degeneracy in the analysis of strong lens systems is to use quasar microlensing which directly measures the stellar mass function at the image position (e.g. Oguri, Rusu & Falco 2014; Schechter et al. 2014; Jiménez-Vicente et al. 2015).

The sample assembled by the SLACS team has shown that lensing galaxies are indistinguishable from non-lensing ETGs with similar velocity dispersions in terms of their internal properties and environment (Bolton et al. 2006; Koopmans et al. 2006; Treu et al. 2006; Gavazzi et al. 2007; Bolton et al. 2008; Auger et al. 2009, 2010; Koopmans et al. 2009; Treu et al. 2009; Barnabè et al. 2011; Czoske et al. 2012; Shu et al. 2015). Additional samples of higher redshift lenses with measured velocity dispersion have then been built, such as the Strong Lensing Legacy Survey (Tu et al. 2009; Ruff et al. 2011a; Gavazzi et al. 2012; Sonnenfeld et al. 2013a,b, 2015; Gavazzi et al. 2014) or BOSS Emission-line Lens Survey (Bolton et al. 2012; Brownstein et al. 2012; Shu et al. 2016) and allowed one to investigate the time dependence of the slope of the inner total mass density profile near the effective radius (see also Dye et al. 2014; Tortora et al. 2014; Posacki et al. 2015; Smith, Lucey & Conroy 2015). At fixed mass, the total density slope correlates with the projected stellar mass density and seems to decrease with redshift while remaining close to isothermal ($\gamma' \equiv -\mathrm{dlog}\,\rho/\mathrm{dlog}\,r \simeq 2$, with a noticeably small ∼6 per cent intrinsic scatter). Similar conclusions can be drawn from spatially resolved stellar kinematics of ETGs (see e.g. Cappellari 2016, for a review). In addition, the combination of strong lensing and stellar kinematics at group and cluster scales can also provide us with sizable statistical samples (Newman et al. 2013; Newman, Ellis & Treu 2015) for extending our understanding of galaxy formation towards the high-mass end.

In parallel to these observational efforts, several attempts were made to understand the origin and the tightness of this relation, either with semi-analytical models or idealized simulations (Nipoti et al. 2009; Lackner & Ostriker 2010; Hirschmann et al. 2012; Johansson, Naab & Ostriker 2012; Lackner et al. 2012; Nipoti et al. 2012; Remus et al. 2013; Dutton & Treu 2014; Sonnenfeld, Nipoti & Treu 2014; Shankar et al. 2017). The complex coupling of scales (from DM haloes and beyond to star formation and AGN activity) involved for understanding this dynamical interplay between baryons and DM haloes requires very demanding numerical hydrodynamical simulations. An important step forward was made possible by zoomed hydrodynamical simulations around massive galaxies that contain realistic accretion scenarios and sufficient resolution to recover with good fidelity the internal structure of massive ETGs (Dubois et al. 2013). In particular, a detailed census on the role of the feedback from the central AGN was made, showing that the quenching of star formation by the central engine is not only important for reproducing stellar to halo mass relations and colours but also for reproducing the size and the dynamical structure (pressure support instead of rotation). The small statistics permitted with these zooms has recently been alleviated by a hydrodynamical simulation with RAMSES (Teyssier 2002) of larger cosmological volumes containing 10^5 objects with similar resolution. This was one of the purposes of the HORIZON-AGN ($H_{\rm AGN}$) simulation (Dubois et al. 2014, 2016; Beckmann et al. 2017; Kaviraj et al. 2017; Welker et al. 2017), who confirmed with better statistics some of the results of Dubois et al. (2013).

Recently, a comparison of the internal structure of massive ETGs in the Illustris Simulation (Vogelsberger et al. 2014) which is quite comparable to $H_{\rm AGN}$ showed reasonable agreement with observations, although the size of galaxies seems to be slightly overshot (Xu et al. 2017). This confirms the interest in performing detailed comparisons between simulations and observations with different simulation codes and solvers in order to study degeneracies between subgrid physical recipes and solver specificities that could match observations for very different physical reasons. Hence, since we already studied in detail the role of AGN feedback on the evolution of internal DM and stellar density profiles from our set of ($H_{\rm AGN}$) simulations (Peirani et al. 2017), we will now attempt to compare our results with the SLACS + SL2S lensing observational constraints on the internal structure of massive galaxies coming from strong lensing and dynamics, the main focus being the total mass density profile within the effective radius.

The paper is organised as follows. Section 2 briefs the numerical modelling used in this work (simulations and post-processing) while Section 3 presents our main results relative to the evolution of the total density profiles in massive ETGs. We finally conclude in Section 4.

2 NUMERICAL MODELLING

In this paper, we analyse and compare galaxy samples extracted from two large cosmological hydrodynamical simulations, HORIZON-AGN ($H_{\rm AGN}$) and HORIZON-NOAGN ($H_{\rm noAGN}$). These simulations and galaxies/DM haloes samples production have been already described in great details in Dubois et al. (2014, 2016) and Peirani et al. (2017). In the following, we only summarize the main features.

2.1 HORIZON-AGN and HORIZON-NOAGN

The $H_{\rm AGN}$ simulation (Dubois et al. 2014) considers a standard ΛCDM cosmology with total matter density $\Omega_{\rm m} = 0.272$, dark energy density $\Omega_\Lambda = 0.728$, amplitude of the matter power spectrum $\sigma_8 = 0.81$, baryon density $\Omega_{\rm b} = 0.045$, Hubble constant $H_0 = 70.4\,{\rm km\,s^{-1}\,Mpc^{-1}}$, and $n_s = 0.967$ compatible with the WMAP-7 (Komatsu et al. 2011). The simulation was performed in a periodic box of side $L_{\rm box} = 100\,h^{-1}$ Mpc containing 1024^3 DM particles, resulting in a DM mass resolution of $M_{\rm DM,res} = 8.27 \times 10^7\,{\rm M}_\odot$. The

simulation is run with the RAMSES code (Teyssier 2002), and the initially uniform grid is adaptively refined down to $\Delta x = 1$ proper kpc at all times.

$H_{\rm AGN}$ includes gas dynamics, gas cooling, and heating (from an uniform UV background taking place after redshift $z_{\rm reion} = 10$), and various sub-grid models such as: star formation, feedback from stars (stellar winds, type Ia and type II supernovae), metal enrichment of the interstellar medium by following six chemical species (O, Fe, C, N, Mg, Si). BH formation and growth are also included. We consider a Bondi–Hoyle–Lyttleton accretion rate on to BHs namely $\dot{M}_{\rm BH} = 4\pi\alpha G^2 M_{\rm BH}^2 \overline{\rho}/(\overline{c}_s^2 + \overline{u}^2)^{3/2}$, where $M_{\rm BH}$ is the BH mass, ρ the mean gas density, $\overline{c}_s$ the average sound speed, $\overline{u}$ the average gas velocity relative to the BH velocity, and α a dimensionless boost factor defined by $\alpha = (\rho/\rho_0)^2$ when $\rho > \rho_0$ and $\alpha = 1$ otherwise (Booth & Schaye 2009). The effective accretion rate on to BHs is capped at the Eddington accretion rate: $\dot{M}_{\rm Edd} = 4\pi G M_{\rm BH} m_p/(\epsilon_r \sigma_T c)$ in which c is the speed of light, $m_{\rm p}$ the proton mass, σ_T the Thompson cross-section, and ε_r the radiative efficiency. In our modelling, we assumed $\varepsilon_r = 0.1$ for the Shakura & Sunyaev (1973) accretion on to a Schwarzschild BH. BHs release energy in two distinct modes: quasar (heating) or radio (kinetic jet) mode when the accretion rate $\chi \equiv \dot{M}_{\rm BH}/\dot{E}_{dd}$ is $\chi > 0.01$ and $\chi < 0.01$, respectively. The quasar mode is modelled as an isotropic injection of thermal energy into the gas within a sphere of radius Δx and at an energy deposition rate $\dot{E}_{\rm AGN} = \epsilon_f \epsilon_r \dot{M}_{\rm BH} c^2$, where $\varepsilon_f = 0.15$ is a free parameter used to match the BH–galaxy scaling relations (see Dubois et al. 2012 for detail). At low accretion rates, energy is released through AGN radio mode into a bipolar outflow with a jet velocity of 10^4 km s^{-1}. Following Omma et al. (2004), a cylinder with a cross-sectional radius Δx and height $2\Delta x$ is used to model the outflow (see Dubois et al. 2010 for details). In this case, the efficiency of the radio mode is larger than the quasar mode with $\varepsilon_f = 1$. In fig. 5 of Peirani et al. (2017), we have studied the evolution of the Eddington ratio χ over relevant DM halo mass ranges. Our results strongly indicate that the radio mode tends to be the dominant mode below $z \lesssim 2$. These results are also in agreement with Volonteri et al. (2016) who have studied in detail the cosmic evolution of BHs in the HORIZON-AGN simulation.

$H_{\rm NOAGN}$ was performed using the same set of initial conditions and sub-grid modelling but with no BH formation and therefore no AGN feedback. The stellar feedback has not been changed between the two simulations, and we insist on the fact that the stellar feedback in $H_{\rm AGN}$ is not 'tuned' to match any galaxy properties. In both simulations, the stellar mass resolution is $M_{*,\rm res} = 2 \times 10^6$ M$_\odot$.

Finally, it is worth mentioning that the $H_{\rm AGN}$ simulation has been extensively analysed in order to make theoretical predictions to be compared to observational data. In particular, the statistical properties of the simulated galaxies have been studied, showing good agreement with observed stellar mass functions all the way to $z \sim 6$ (Kaviraj et al. 2017). The colour and star formation histories are also well recovered as well as the so called BH–bulge relations and duty-cycles of AGNs (Volonteri et al. 2016).

2.2 Galaxy catalogues

Galaxies are identified using the ADAPTAHOP (sub)halo finder (Aubert, Pichon & Colombi 2004) and for this study, we mainly focus on galaxies with a mass greater than 10^{11} M$_\odot$. We use also the most bound particle as the definition of their centre. For each given $H_{\rm AGN}$ or $H_{\rm noAGN}$ galaxy, we compute the radial, tangential and vertical velocity components of each stellar particle where the orientation of the z-axis cylindrical coordinate is defined by the spin vector (i.e. the angular momentum vector from the stellar component). Then, we estimate the rotational velocity V of the galaxy by computing the average of the tangential velocity component. The velocity dispersion σ is obtained from the dispersion of the radial σ_r, the tangential σ_θ and the vertical velocity σ_z components around their averaged values namely $\sigma^2 = (\sigma_r^2 + \sigma_\theta^2 + \sigma_z^2)/3$. In our analysis, we select in general $H_{\rm AGN}$ and $H_{\rm noAGN}$ galaxies with $V/\sigma < 1$ because we are interested in ETGs only.

Finally, in order to match galaxies between $H_{\rm AGN}$ and $H_{\rm noAGN}$ simulations, we use the scheme developed in Peirani et al. (2017). To summarize, we first match host DM haloes between the two simulations. To do so, we use the fact that, as we start from the same initial conditions, each DM particle possesses an identity which is identical among the twin simulations. Then, if more than 75 per cent of the particles of any given halo in the $H_{\rm AGN}$ can also be found in a halo identified in the $H_{\rm NOAGN}$, we conclude that these haloes are associated (provided that their mass ratio is lower than 10 or greater than 0.1). This scheme cannot be repeated to match galaxies since stellar particles are created during the simulations and do not necessarily correspond between the two runs. Therefore, we first couple each galaxy to a host DM halo in their parent simulation by choosing the most massive galaxy whose centre is located within a sphere of radius equal to 5 per cent of the virial radius of its host halo. Galaxy pairs between the two simulation are then determined through the matching of their host halo as previously described. Note that past numerical works suggest that the presence of AGN feedback allows mergers to durably transform rotationally supported discs ($V/\sigma > 1$) into dispersion-dominated ellipsoids ($V/\sigma < 1$) (Dubois et al. 2013, 2016). Therefore, when using our matching algorithm, $H_{\rm AGN}$ galaxies satisfying $V/\sigma < 1$ might be associated to $H_{\rm noAGN}$ galaxies with $V/\sigma > 1$.

3 THE TOTAL DENSITY SLOPES AT THE EFFECTIVE RADIUS

3.1 Definitions

In this study, we focus on the *mass-weighted density slope within r_1 and r_2* introduced by Dutton & Treu (2014):

$$\gamma' = \frac{1}{M(r_2) - M(r_1)} \int_{r_1}^{r_2} \gamma(x) 4\pi x^2 \rho(x)\, {\rm d}x, \quad (1)$$

where $\gamma \equiv -{\rm d}\log\rho\ /{\rm d}\log r$ is the local logarithmic slope of the density profile ρ and M the local mass. Using a discrete representation of each density profile, $\gamma(r)$ and $M(r)$ can be estimated within each radial bin.

For each studied galaxy, we have considered a random orientation in space and then derive the effective radius $R_{\rm e}$ at which half of the projected stellar mass is enclosed. Finally, in order to estimate γ' at $R_{\rm e}$, we consider the interval $[r_1 - r_2] = [R_{\rm e}/2 - R_{\rm e}]$ since it corresponds to radii probed by the strong lens samples used in this paper. In strong lensing + dynamics studies, the total density slope γ' is observationally determined by fitting a power-law density profile to the Einstein radius and central velocity dispersion (Koopmans et al. 2006). Strictly speaking, the value of γ' recovered in this way is equal to the mass-weighted slope of the lens only if its true density profile is a power law. Nevertheless, Sonnenfeld et al. (2013b) showed how these two definitions of the slope give values of γ' that are typically within 0.05 of each other, for a variety of lens density profiles (see also Xu et al. 2017, for a detailed study). Note also that the simulation grid size has a value of 1 kpc where DM or galaxy density profiles might not fully converge. In Appendix A, we have

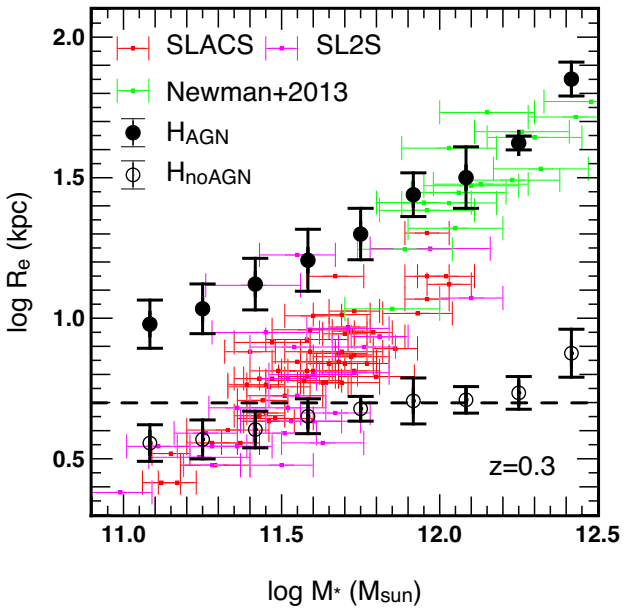

Figure 1. The variations of the effective radius R_e with respect to the stellar mass M_*. Results are derived from H_{AGN} (black points) and H_{noAGN} (white points) galaxies satisfying $V/\sigma < 1$ and $\log(M_*/M_\odot) > 11$ at $z = 0.3$. We also plot observational data from the SLACS, SL2S, and Newman et al. (2013) which cover the redshift range of $[0.063 - 0.884]$ but centred around $z \sim 0.3$. Errorbars indicate the 1σ standard deviations using a confidence interval on the scatter in a bin. For indicative purposes only, the horizontal dashed lines at R_e =5 kpc indicates a recommended resolution limit following Power et al. (2003).

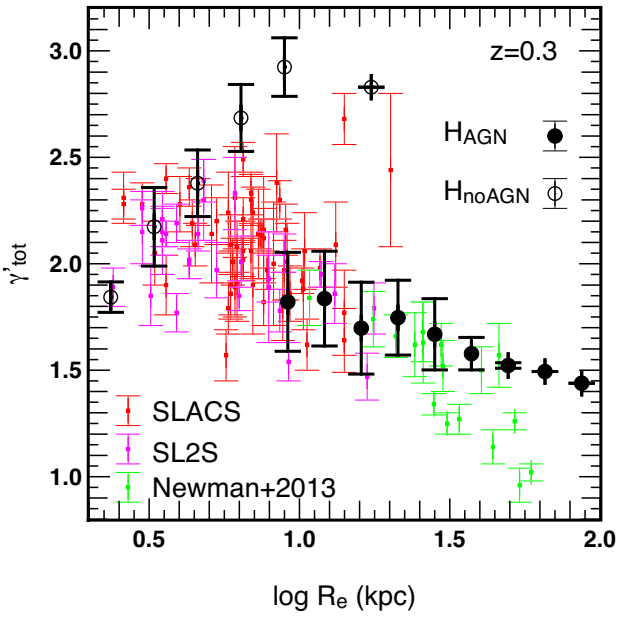

Figure 2. The variations of the mass-weighted total density slopes γ'_{tot} with respect to the effective radius R_e. Results are derived from H_{AGN} (black points) and H_{noAGN} (white points) galaxies with $V/\sigma < 1$ and a mass of $\log(M_*/M_\odot) > 11$ at $z = 0.3$. We also plot observational data from SLACS (red colours), SL2S (pink colours) and Newman et al. (2013) (green colours). Error bars indicate 1σ standard deviations. AGN feedback is again required to improve the agreement between theoretical predictions and observational trends.

performed a convergence study in the same way than Duffy et al. (2010) and found that the lower limit value of 5 kpc recommended by Power et al. (2003) for our studied halo/galaxy mass range, is suitable in our analysis, though their work concerns pure DM simulations only. In general, the effective radius of H_{AGN} galaxies is always larger than 5 kpc. However, this is not the case for H_{noAGN} galaxies and therefore, in certain cases, we will remove galaxies with too low effective radii (i.e. $R_e/2 \leq 1$–2 kpc).

In the following, we will refer, respectively, to γ'_{dm}, γ'_*, and γ'_{tot} the mass-weighted density slope derived from the DM component, the stellar component, and the DM + stellar components.

3.2 Dependencies of γ'_{tot} with R_e, M_{halo}, and M_*

Fig. 1 shows the variations of the effective radius R_e with respect to the stellar mass M_* for H_{AGN} and H_{noAGN} galaxies with a mass greater than $10^{11}\,M_\odot$ and $V/\sigma < 1$ at $z = 0.3$. We chose this latter redshift value because the observational data we want to compare with, in particular SLACS, SL2S, and Newman et al. (2013, 2015), are centred around this value. The observed values of the stellar mass depend upon the assumption of a stellar IMF. For our comparison we assume a Salpeter IMF, which is found to be consistent with stellar masses derived from the combination of lensing and dynamics in the sample of SLACS and SL2S lenses (Sonnenfeld et al. 2015). First, we see clearly that in the absence of AGN feedback, the simulated galaxies are generally clearly too compact with an effective radius too small, compared to observational data. Note however that for H_{noAGN} galaxies with $\log(M_*/M_\odot) < 11.5$, the theoretical predictions seems to agree well with observations. This might be due to the fact that as the effective radius get closer to the resolution limit, their value might be overestimated. On the contrary, AGN feedback tends to form more extended galaxies as already noted by Dubois et al. (2013). In this case, high-mass ellipticals in H_{AGN} are in good agreement with the observations while low-mass ellipticals seem to be not compact enough. This effect could be attributed again to limited spatial resolution, as the size of low-to-intermediate mass galaxies is only a few times the spatial resolution, and can get some spurious dynamical support. Therefore, galaxy sizes are supposed to converge to $\Delta x = 1$ kpc at the low-mass end, and it is well plausible that the low-mass galaxies will get more compact with increased spatial resolution. Also, it is worth mentioning that the lensing probability p is a steep function of the velocity dispersion of galaxies σ (i.e. $p \approx \sigma^4$). Then, for a given stellar mass, more compact galaxies will be selected by using survey which can partly explain the discrepancies between theoretical predictions and observations here. In the following, in order to take into account this selection effect, estimations of the mean value of γ'_{tot} are weighted by σ^4. However, no significant difference is noticed in the results and conclusions when γ'_{tot} values are derived without this weighting.

Fig. 2 shows now the variations of the mass-weighted total density slope γ'_{tot} with respect to the effective radius R_e at $z = 0.3$ for H_{AGN} and H_{noAGN} galaxies with a mass greater than $10^{11}\,M_\odot$ and $V/\sigma < 1$. When comparing our results to observations, we get a much better agreement when AGN feedback is taken into account. Indeed, we found that γ'_{tot} derived from H_{AGN} simulation is decreasing with R_e which is consistent with the observational trend. On the contrary, an opposite evolution is obtained when AGN are not included suggesting that more extended galaxies (or more massive galaxies) tend to have higher γ'_{tot} values. Moreover, for $R_e \geq 10$ kpc, the predicted γ'_{tot} values derived from the H_{AGN} simulation are in

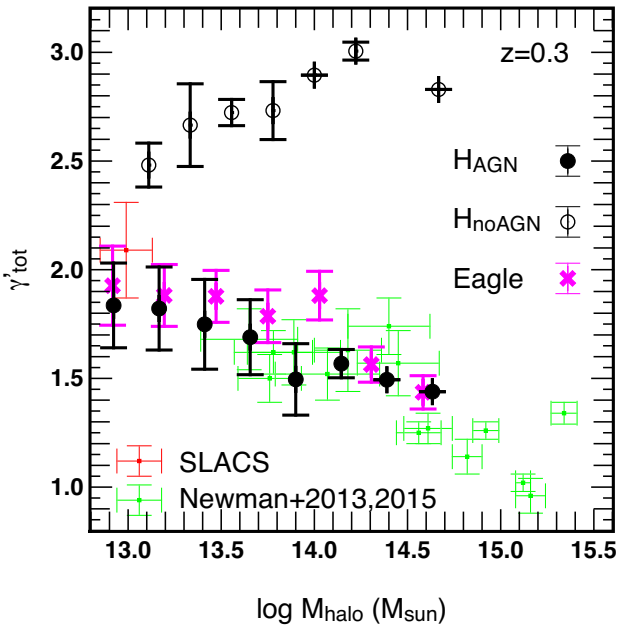

Figure 3. The variations of the mass-weighted total density slopes $\gamma'_{\rm tot}$ with respect to the DM halo masses $M_{\rm halo}$. Results are derived from $H_{\rm AGN}$ (black points) and $H_{\rm noAGN}$ (white points) galaxies with $V/\sigma < 1$ and a mass of $\log(M_*/{\rm M}_\odot) > 11$ at $z = 0.3$. We also plot observational data from SLACS (red colours) and Newman et al. (2013, 2015) (green colours) as well as predictions from the Eagle simulation. Errorbars indicate 1σ standard deviations. When AGN feedback is included, theoretical predictions are in nice agreement with observations. On the contrary, in the absence of AGN feedback, derived $\gamma'_{\rm tot}$ values are totally inconsistent with observational expectations.

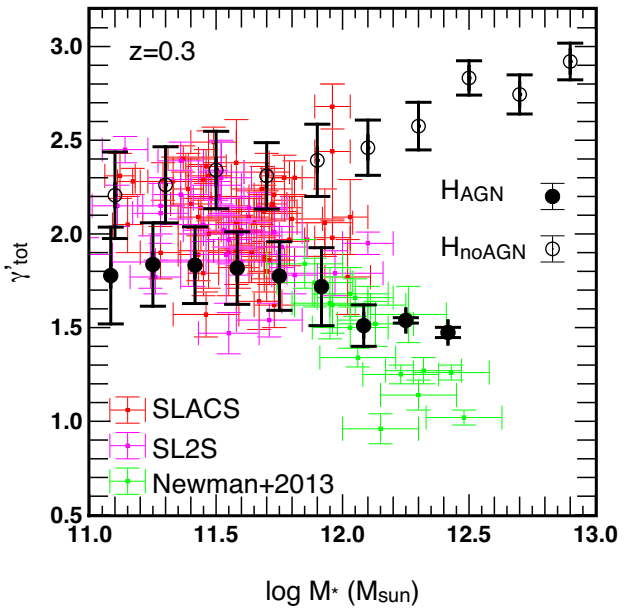

Figure 4. The variations of the mass-weighted total density slopes $\gamma'_{\rm tot}$ with respect to the stellar masses M_* at $z = 0.3$. Results are derived from $H_{\rm AGN}$ (black points) and $H_{\rm noAGN}$ (white points) galaxies with $V/\sigma < 1$ and a mass of $\log(M_*/{\rm M}_\odot) > 11$. We also plot observational data from SLACS (red colours), SL2S (pink colours) and Newman et al. (2013) (green colours). Errorbars indicate 1σ standard deviations. AGN feedback seems to reproduce the observations well.

good agreement with those of observations. In particular, we get density slopes close to 2 for the less massive galaxies of our sample which are values expected from the observations. We cannot match the observations for $R_{\rm e} < 10$ kpc since $H_{\rm AGN}$ low-mass elliptical galaxies are too extended as shown in Fig. 1.

Our comparison between the predicted and observed mass–size relation also depends on the assumption of the stellar IMF. The data points plotted in Fig. 1 are based on a Salpeter IMF. However, a recent re-analysis of SLACS lenses shows how the presence of gradients in stellar mass-to-light ratio, required by the data, can decrease the inferred stellar masses by as much as 0.2 dex compared to the Sonnenfeld et al. (2015) values (Sonnenfeld et al. 2018). If the values of the stellar masses of SLACS lenses decrease, the data points would move in better agreement with the $H_{\rm AGN}$ simulation.

From the same samples of galaxies at $z = 0.3$ (i.e. $M_* \geq 10^{11}$ M$_\odot$ and $V/\sigma < 1$), we also take an interest in studying the variations of $\gamma'_{\rm tot}$ with respect to either the DM halo masses $M_{\rm halo}$ or stellar masses M_*. Those variations are displayed in Figs 3 and 4, respectively. We find similar trends to those obtained in Fig. 2. First, the presence or not of AGN feedback leads to opposite evolution trends. When AGN feedback is included, $\gamma'_{\rm tot}$ is decreasing with $M_{\rm halo}$ or M_*. In other words, more massive objects tend to have more flat total density profiles at the scale of the effective radius. A similar conclusion was obtained in Peirani et al. (2017), when studying the inner DM and stellar profiles ($r \leq 5$ kpc) which is mainly explained by the fact that AGN feedback has a more important impact in the most massive objects. Moreover, values of $\gamma'_{\rm tot}$ are in good agreement with observational ones. On the contrary, in the absence of AGN feedback, $\gamma'_{\rm tot}$ values are much too high especially for massive objects. Note that we didn't use our matching scheme here when selecting the $H_{\rm noAGN}$ galaxies in order to consistently compare with the observational mass range. However, we have checked that the matching scheme would select $H_{\rm noAGN}$ galaxies with higher masses and higher effective radius but will not really change the evolutions of $\gamma'_{\rm tot}$ previously derived. It is also encouraging to notice that our simulated values for $H_{\rm AGN}$ haloes presented in Fig. 3 are in good agreement with those of Schaller et al. (2015) using the Eagle simulation (Schaye et al. 2015). In Appendix A, we also compare the results from lower resolution simulations. We found good agreement in the different trends relative to the variations of $\gamma'_{\rm tot}$ with respect to the effective radius, the DM halo masses and the stellar masses though there are some slight discrepancies in the variations of the effective radius with respect to the stellar masses.

In view of all of these results, AGN feedback seems to be required to explain the observational trends.

3.3 Dependencies of $\gamma'_{\rm tot}$ with $\gamma'_{\rm dm}$ and γ'_*

In this section, we investigate the variations of $\gamma'_{\rm tot}$ with either the stellar slope γ'_* or the DM slope $\gamma'_{\rm dm}$ for galaxies with a mass greater than 10^{11} M$_\odot$ and $V/\sigma < 1$ at $z = 0.3$. Results from $H_{\rm AGN}$ and $H_{\rm NOAGN}$ simulations are presented in Fig. 5. First, when AGN feedback is included, one can notice that $\gamma'_{\rm tot}$ and $\gamma'_{\rm dm}$ are strongly correlated. Regarding the dependence of $\gamma'_{\rm tot}$ and γ'_*, the dispersion is higher and the correlation is less clear but the important point here is that AGN feedback tends to limit the total slope to values close to 2 for the less massive galaxies while it reduces $\gamma'_{\rm tot}$ in the more massive ones compared to the simulation without AGN, which is consistent with the observations. On the contrary, in the absence of AGN feedback, we found again the opposite trends: $\gamma'_{\rm tot}$ and γ'_* are this time strongly correlated and due to stronger adiabatic contraction,

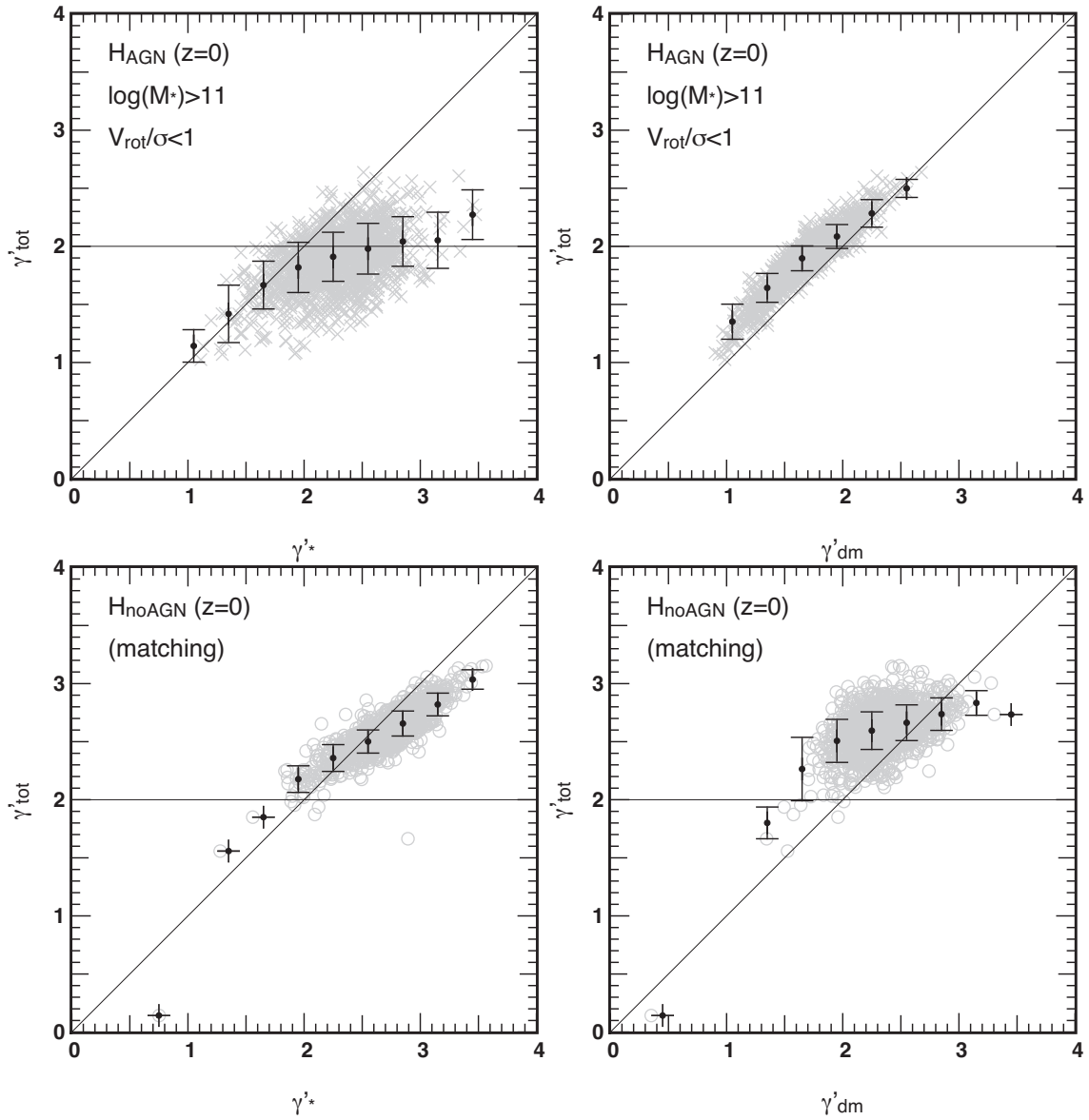

Figure 5. First line: The variations of the mass-weighted total density slope $\gamma'_{\rm tot}$ with respect to the mass-weighted stellar density slope γ'_* (first column) or the mass-weighted DM density slope $\gamma'_{\rm dm}$ (second column) for $H_{\rm AGN}$ galaxies with a mass greater than 10^{11} M$_\odot$ and $V/\sigma < 1$ at z = 0. Results from the matching $H_{\rm noAGN}$ galaxies are displayed in the second line. The horizontal solid line represents $\gamma'_{\rm tot} = 2$ generally obtained in the observation while the diagonal one is $y = x$.

$\gamma'_{\rm dm}$ reach values too high in more massive objects (see Peirani et al. 2017).

Another way to look into those variations and potential strong correlations between the three different density slopes is to consider the two-dimensional plots of Fig. 6 showing the variations of γ'_* and $\gamma'_{\rm dm}$ with a colour code representing the values of $\gamma'_{\rm tot}$ for galaxies with a mass greater than 10^{11} M$_\odot$ and $V/\sigma < 1$ at $z = 0$. Note that this time we use the matching algorithm to select the $H_{\rm noAGN}$ galaxies which has the advantage, beside comparing the same objects between the simulations, to us to consider a higher number of $H_{\rm noAGN}$ galaxies. Indeed, most of the massive $H_{\rm noAGN}$ galaxies are disc-dominated and do not then satisfied $V/\sigma < 1$ (see Dubois et al. 2016). However, we have checked that no significant differences are obtained if $H_{\rm noAGN}$ galaxies were selected using the same mass and V/σ criteria. Thus, the plots presented in Fig. 6 give the possible pairs $(\gamma'_{dm}, \gamma'_*)$ for a given value of $\gamma'_{\rm tot}$. We also see the linear correlations between $\gamma'_{\rm tot}$ and $\gamma'_{\rm dm}$ and between $\gamma'_{\rm tot}$ and γ'_* when AGN is included or not, respectively.

The strong correlations seen between $\gamma'_{\rm tot}$ and $\gamma'_{\rm dm}$ or $\gamma'_{\rm tot}$ and γ'_* when AGN is included or not, respectively, can be easily understood when studying the density profile of the different components of a single object shown in Fig. 7. When AGN are included, galaxies are more extended and therefore have higher effective radii in general. Consequently, the DM is the dominant component at the effective radius scale. On the contrary, galaxies are found to be very compact in the absence of AGN activity and have therefore a smaller effective radius. In this case, the stellar component is the dominant component at the effective radius scale as is clearly shown in Fig. 7.

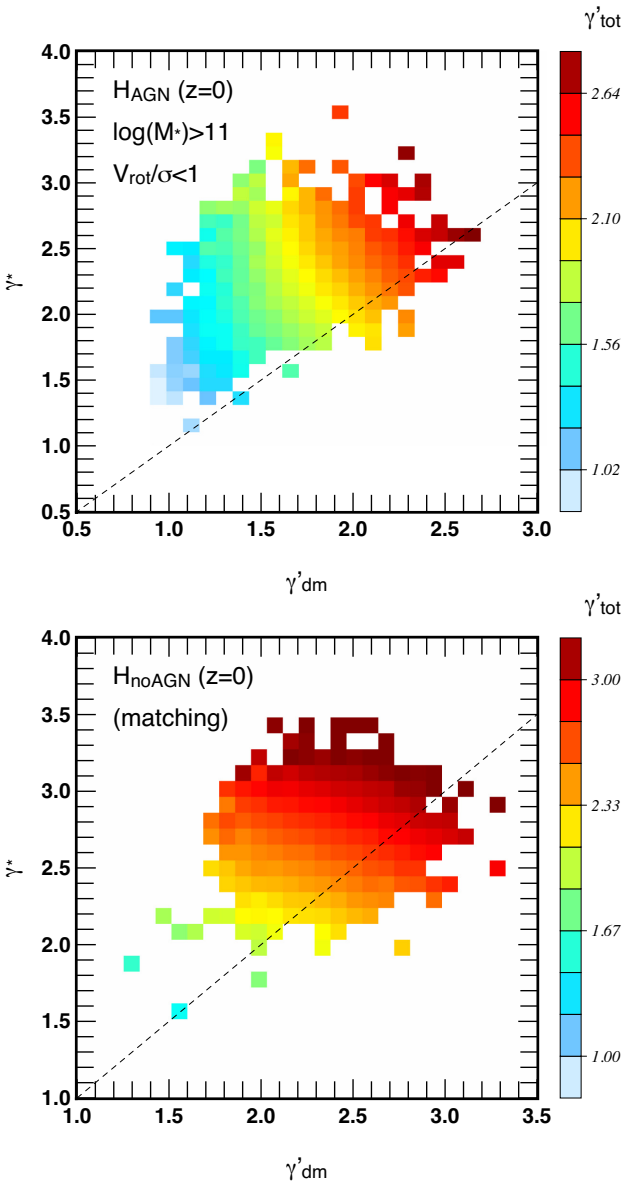

Figure 6. The variations of the mass-weighted stellar density slope γ'_* with respect to the mass-weighted DM density slope $\gamma'_{\rm dm}$ for $H_{\rm AGN}$ galaxies with a mass greater than 10^{11} $M_\odot$ and $V/\sigma < 1$ at $z = 0$ (upper panel) and matching $H_{\rm noAGN}$ galaxies (lower panel). The colour code represents values of the mass-weighted total density slope $\gamma'_{\rm tot}$. The dashed line indicates $y = x$.

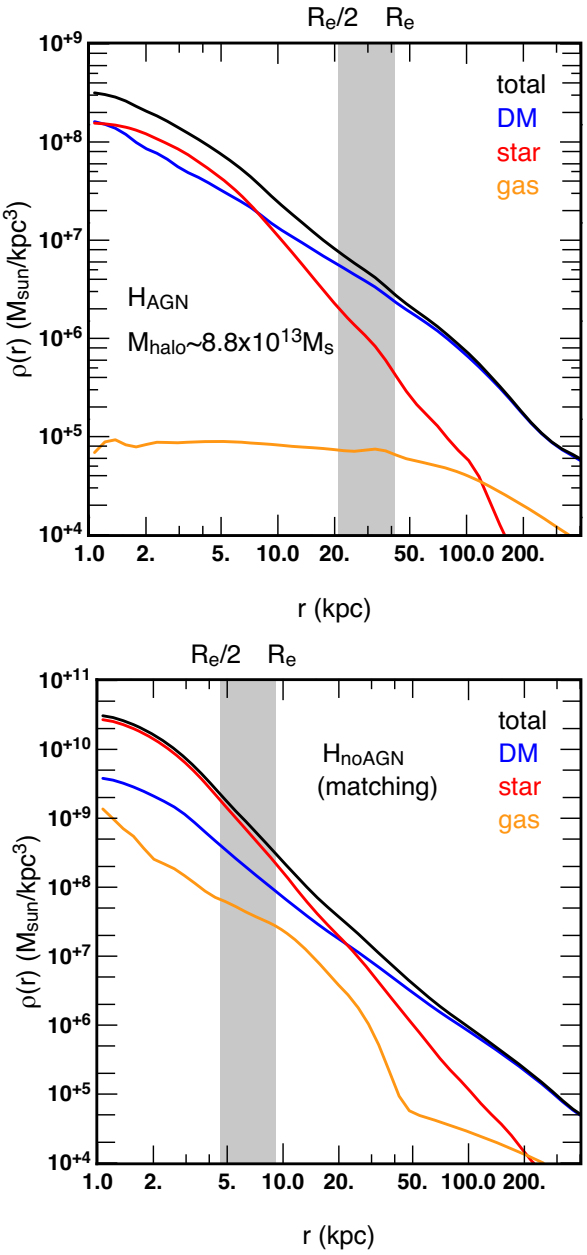

Figure 7. The total density profile (black lines) of the same massive DM halo extracted from the $H_{\rm AGN}$ (upper) and $H_{\rm NOAGN}$ (lower) simulations at $z = 0$. The DM, stellar, and gas components are also shown in blue, red, and orange colours, respectively. The grey shade areas indicate the range of $[R_e/2 - R_e]$, i.e. where we compute $\gamma'_{\rm tot}$, γ'_*, and $\gamma'_{\rm dm}$.

3.4 Evolution of $\gamma'_{\rm tot}$ between $0 \leq z \leq 2$

One of the main objectives of this paper is to make theoretical predictions of the time evolution of $\gamma'_{\rm tot}$ of massive ETGs. Fig. 8 presents the time evolution of $\gamma'_{\rm dm}$, γ'_*, and $\gamma'_{\rm tot}$ for $H_{\rm AGN}$ galaxies with a mass greater than 10^{11} $M_\odot$ and $V/\sigma < 1$ in the redshift range $0 \leq z \leq 2$. We also impose $R_e > 5$ kpc in order to be not too close to the lower resolution limit. We also derived the evolution for associated $H_{\rm noAGN}$ galaxies. Note that we analyse here the evolution from $z = 2$ since our resolution does not enable us to properly estimate the different density slopes at higher z as typical effective radii of galaxies at higher redshift become too small. When considering $H_{\rm AGN}$ galaxies, we see a slight increase with time of the DM and total density slopes while the stellar density slope is nearly constant and close to 2.3 in the considered redshift interval. This means that the DM and total density profiles estimated at the effective radius tend to become slightly steeper at low redshifts while the stellar one does not vary significantly. The situation is slightly different for matching $H_{\rm noAGN}$ galaxies. In this case, contrary to $\gamma'_{\rm dm}$ which is increasing, γ'_* and therefore $\gamma'_{\rm tot}$ seem to be almost constant after $z = 1$. Note that an additional level of refinement occurs at $z \sim 0.25$. The extra star formation spuriously induced at this epoch increases the central stellar mass, and induces a bump in the evolutions of γ'_*, $\gamma'_{\rm dm}$ (by adiabatic contraction) and therefore $\gamma'_{\rm tot}$. But despite this, it appears clearly that when AGN is not taken into account, the density slopes of each component is always higher than $H_{\rm AGN}$ counterparts.

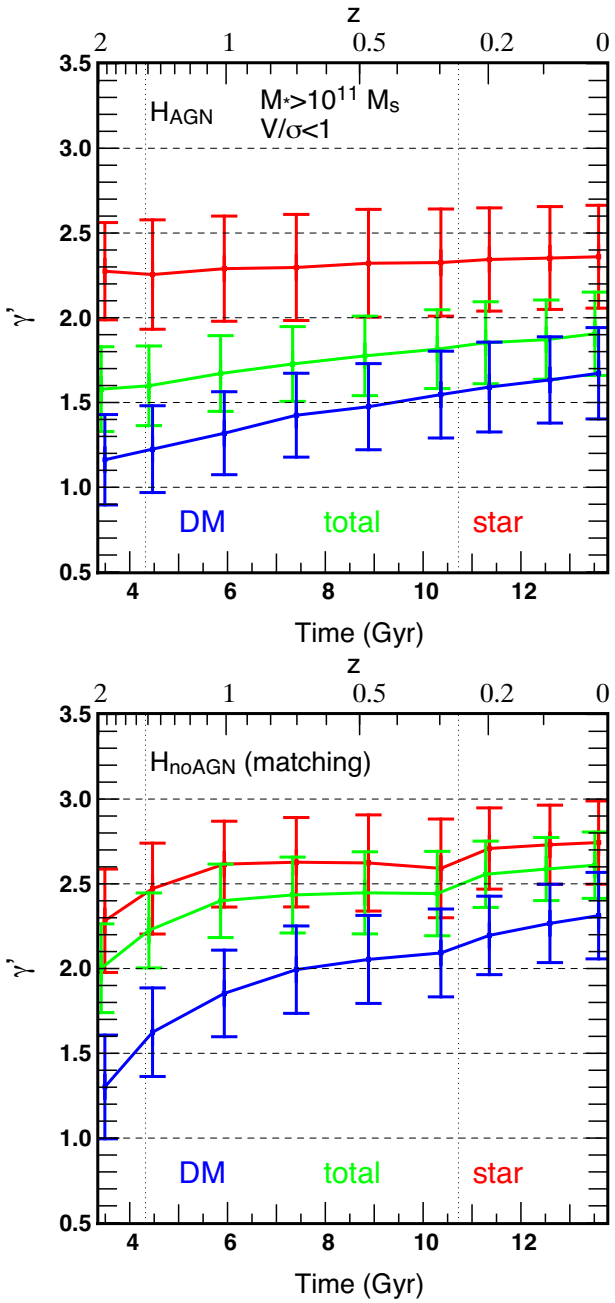

Figure 8. First line: The time evolutions of the mass-weighted total density slope $\gamma'_{\rm tot}$ (green lines) for $H_{\rm AGN}$ galaxies with $V/\sigma < 1$, a mass greater than 10^{11} $M_\odot$ and $R_{\rm e} > 5$ kpc. We also show the variations of the stellar (γ'_*) and DM ($\gamma'_{\rm dm}$) components in red and blue lines, respectively. The same evolutions obtained from the matching $H_{\rm noAGN}$ galaxies are displayed in the second line. Errorbars are 1σ standard deviations. The vertical dotted lines indicate the times when a new refinement level is added in the simulations.

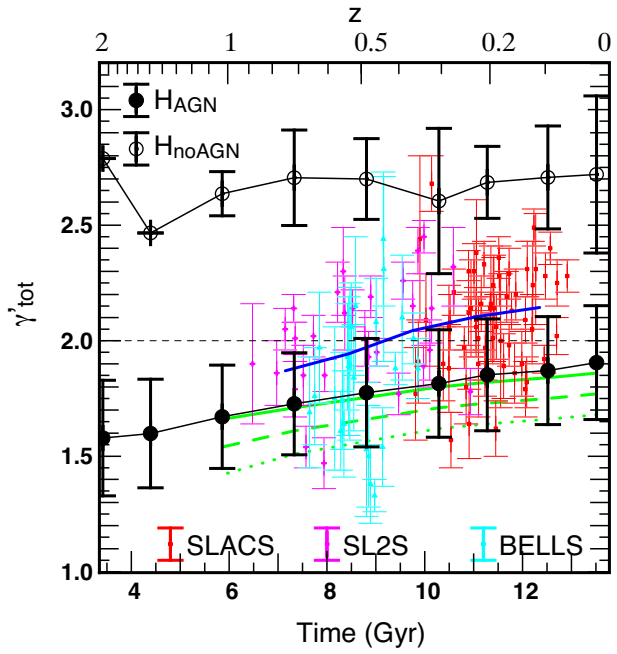

Figure 9. The time evolutions of the mass-weighted total density slope $\gamma'_{\rm tot}$ for $H_{\rm AGN}$ (black points) and $H_{\rm noAGN}$ (white points) galaxies satisfying $V/\sigma < 1$, $M_* \geq 10^{11}$ $M_\odot$ and $R_{\rm e} > 5$ kpc in the considered redshift interval. We also add the observational data from the SLACS (red), SL2S (purple), and BELLS (cyan). The solid blue line shows the mean evolution derived from all observational data. The solid, dashed, and dotted green lines are derived from, respectively, the 84, 50, and 16 percentiles of the probability distribution function of $< \gamma'_{\rm tot} >$ from equation (2). They represent the mean evolutions of $\gamma'_{\rm tot}$ after removing the dependence on stellar mass density (see details in the text). Errorbars are 1σ standard deviations.

Finally, we directly compare the evolution of $\gamma'_{\rm tot}$ to observations in Fig. 9. We consider here again galaxies satisfying $M_* \geq 10^{11}$ $M_\odot$, $V/\sigma < 1$ and $R_{\rm e} > 5$ kpc in the redshift range of $0 \leq z \leq 2$. In the absence of AGN feedback, the derived $\gamma'_{\rm tot}$ values are too high compared to observations, as expected. When AGN feedback is included, the derived $\gamma'_{\rm tot}$ values are this time slightly too low. The observational data suggest that $\gamma'_{\rm tot}$ is also slightly increasing in the interval $0 \leq z \leq 0.8$ though there is a large dispersion in the data. Our theoretical prediction from $H_{\rm AGN}$ exhibits much better agreement but it is not yet fully satisfactory. The discrepancies with observations could be explained by the fact that the $H_{\rm AGN}$ galaxies are too extended as shown in Fig. 1. Having galaxies slightly more compact, especially for the low-mass ellipticals, will tend to increase values of $\gamma'_{\rm tot}$ and therefore improve greatly matching with observations.

For a more accurate comparison between our predictions and observations, we need to take into account the additional dependence of $\gamma'_{\rm tot}$ on stellar mass and size. In other words, at each z, we need to compare the average $\gamma'_{\rm tot}$ of our simulated galaxies with the average $\gamma'_{\rm tot}$ observed for galaxies with the same values of M_* and $R_{\rm e}$. The latter can be obtained by evaluating equation (2) at the same M_* and $R_{\rm e}$ as the simulation average. This gives us a band which is in general different from the simple average over data points. In Fig. 9, we plot the curves relative to the 16, 50, and 84 percentile of the distribution (green lines). One can notice that, after removing the dependence on mass and size, $< \gamma'_{\rm tot} >$ is still increasing and therefore this increase should not be due to the size–redshift evolution of ETGs galaxies.

The slight increase of $\gamma'_{\rm tot}$ in the considered redshift interval seems to be due to the increase of the density slope of the DM component as suggested by Figs 5, 6, and 8. As shown in Peirani et al. (2017), the evolution of the inner part of $H_{\rm AGN}$ haloes exhibit a condensation phase or 'cusp regeneration' from $z \sim 1.6$ down to $z = 0$. This phase is associated with a decrease of the evolution of the mass accretion on to BHs $\dot{M}_{\rm BH} \equiv {\rm d}M_{\rm BH}/{\rm d}t$ and therefore the AGN activity (see

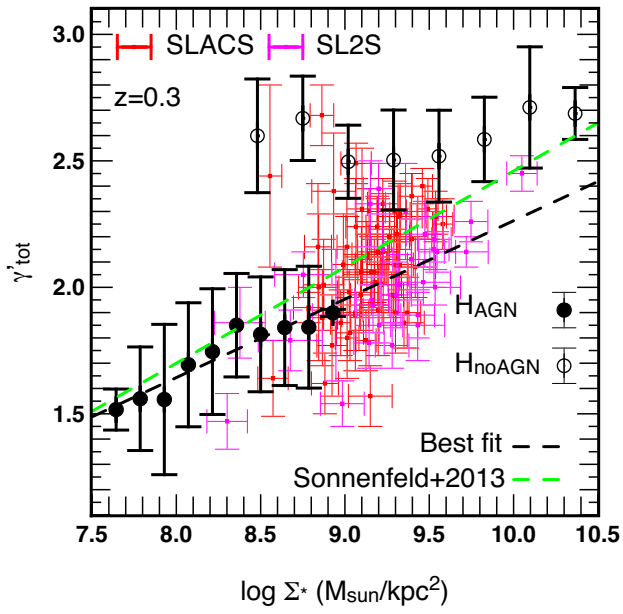

Figure 10. The variations of the mass-weighted total density slopes $\gamma'_{\rm tot}$ as a function of stellar mass density at $z = 0.3$. We consider here the same samples of simulated galaxies than previously. The black dashed line is the best fit measuring the inference on the parameter describing the dependence on Σ_* namely $\eta = 0.31 \pm 0.04$. The green dashed one indicates $\eta = 0.38 \pm 0.07$ derived from observations (see Sonnenfeld et al. 2013b).

fig. 5 in Peirani et al. 2017). Indeed, as advocated by Peirani, Kay & Silk (2008) and Martizzi, Teyssier & Moore (2013), repetitive cycles of gas expansion by AGN feedback (preferably through quasar mode) and gas cooling can efficiently flatten the inner part of DM profiles. If the AGN activity progressively decreases, this proposed mechanism becomes less efficient at counterbalancing the DM adiabatic contraction and at keeping the DM density profiles flat. Note that the density slope of the DM component in the $H_{\rm NOAGN}$ run is also increasing due to the same physical effect namely the adiabatic contraction. However, this not really affect the evolution of the total density profile as this latter mainly depends on the evolution of the stellar component.

Sonnenfeld et al. (2013b) have shown that the dependence of $\gamma'_{\rm tot}$ on the structure of ETGs can be well summarized with a dependence on stellar mass density $\Sigma_* = M_*/(2\pi R_{\rm e}^2)$, leaving little dependence on M_* and $R_{\rm e}$ individually. Equation (2) can then be simplified as follows:

$$< \gamma'_{\rm tot} >= \gamma'_0 + \alpha(z - 0.3) + \eta(\log\Sigma_* - 9). \quad (2)$$

Sonnenfeld et al. (2013b) measured a value of $\eta = 0.38 \pm 0.07$ from the sample of SLACS and SL2S lenses. Our $H_{\rm AGN}$ model is able to reproduce the observed trend with Σ_*, as shown in Fig. 10. By fitting our distribution of $\gamma'_{\rm tot}$ as a function of Σ_* for galaxies at $z = 0.3$, we find $\eta = 0.31 \pm 0.04$, in good agreement with the Sonnenfeld et al. (2013b) value. But once again, since the $H_{\rm AGN}$ galaxies tend to be too extended, the derived Σ_* values are too small compared to the observational values from the same galaxy mass range. This raises an additional question: we have used equation (2) to estimate the observed $\gamma'_{\rm tot}$ for galaxies with the same mass and size as the simulated ones, however there is little overlap in stellar mass density between the SLACS and SL2S lenses and the $H_{\rm AGN}$ galaxies. The use of equation (2) for our simulation is then, strictly speaking, an extrapolation. Nevertheless, Newman et al. (2015) showed how a very similar correlation between $\gamma'_{\rm tot}$ and Σ_* holds down to $\log\Sigma_* = 8.0$. Our use of equation (2) in the stellar mass density regime probed by the $H_{\rm AGN}$ galaxies is then supported by observations.

4 DISCUSSION AND CONCLUSIONS

By comparing results from two state-of-the-art hydrodynamical cosmological simulations whose only difference is the presence/absence of AGN feedback, we have explored the impact of AGN feedback on the evolution of the total density profiles of massive ETGs. We mainly focused on galaxies with a mass greater than $10^{11}\,{\rm M}_\odot$ and satisfying $V/\sigma < 1$. Our findings can be summarized as follows:

(i) In the absence of AGN feedback, the simulated galaxies are clearly too compact with an effective radius too small, compared to observational data. On the contrary, AGN feedback tends to form more extended galaxies as already noted by Dubois et al. (2013, 2016). In this case, high-mass ellipticals in $H_{\rm AGN}$ seem to be in good agreement with the observations while low-mass ellipticals are not compact enough.

(ii) When studying the variations of $\gamma'_{\rm tot}$ with the effective radius, the galaxy mass and the host halo mass at $z = 0.3$, we found that the inclusion of AGN feedback is required to get satisfactory agreement with observational values and trends.

(iii) $\gamma'_{\rm tot}$ is strongly correlated with $\gamma'_{\rm dm}$ when AGN feedback is included. On the contrary, $\gamma'_{\rm tot}$ is strongly correlated with γ'_* in the absence of AGN feedback.

(iv) $\gamma'_{\rm tot}$ is slightly increasing between $0 \leq z \leq 2$. This is due to the fact that when AGN is included, the evolution of $\gamma'_{\rm tot}$ is correlated with the evolution of $\gamma'_{\rm dm}$. In Peirani et al. (2017), we indeed found that the DM density slope is increasing at low redshift because the AGN activity is reduced.

One interesting prediction of the present analysis is the evolution of $\gamma'_{\rm tot}$ over cosmic time. Because of our limited resolution (1 physical kpc), we could only consider the interval $0 \leq z \leq 2$. When AGN are included, we found that $\gamma'_{\rm tot}$ is slightly increasing with time. Compared to observational values, this trend is quite consistent, although the simulated values are slightly too low. This could be explained by the fact that the less massive $H_{\rm AGN}$ galaxies in our samples seem to be too extended. It is worth mentioning that observations from strong lensing by Ruff et al. (2011b) and Bolton et al. (2012) suggest that the total density profile of massive galaxies has become slightly steeper over cosmic time, in agreement with our findings. However, using well-resolved hydrodynamical simulations, Remus et al. (2017) and Xu et al. (2017) found the opposite trend, i.e, $\gamma'_{\rm tot}$ is decreasing after $z = 2$. Probably, the key point here is the behaviour and values of $\gamma'_{\rm tot}$ before $z = 2$. If important sources of feedback (e.g. AGN quasar mode) can flatten the DM and stellar components at high redshift (e.g. Peirani et al. 2008; Martizzi et al. 2013), then it would be difficult to sustain such flat profiles at lower redshift if feedback become less efficient as advocated by Peirani et al. (2017). On the contrary, if these different components are already steep at $z = 2$, then mechanisms such as (dry) major mergers (Sonnenfeld et al. 2014) or efficient feedback could more easily flatten them at low redshift. The observational data of the SLACS, SL2S, and BELLS seems to suggest that $\gamma'_{\rm tot}$ is slightly increasing but future detailed observational data, especially before $z = 2$, will definitely help to constrain the different scenarios and theoretical models.

ACKNOWLEDGEMENTS

We are grateful to the referee Alan R. Duffy and the editor Joop Schaye for giving constructive comments which substantially helped improving the quality of the paper. We warmly thank M. Schaller for providing relevant Eagle simulation data. SP acknowledges support from the Japan Society for the Promotion of Science (JSPS long-term invitation fellowship). This work was granted access to the HPC resources of CINES (Centre Informatique National de l'Enseignement Supérieur) under the allocations 2013047012, 2014047012, and 2015047012 made by GENCI and has made use of the Horizon cluster hosted by the Institut d'Astrophysique de Paris on which the simulation was post-processed. This work is supported in part by JSPS KAKENHI grant number JP26800093, JP15H05892 and JP17K14250 and by World Premier International Research Center Initiative (WPI Initiative), MEXT, Japan. The research of J D is supported by Adrian Beecroft and Science and Technology Facilities Council (STFC). The research of J S has been supported at IAP by ERC project 267117 (DARK) hosted by Université Pierre et Marie Curie - Paris 6. This work was carried out within the framework of the Horizon project (http://www.projet-horizon.fr) and is partially supported by the grants ANR-13-BS05-0005 of the French Agence Nationale de la Recherche.

REFERENCES

Aubert D., Pichon C., Colombi S., 2004, MNRAS, 352, 376
Auger M. W., Treu T., Bolton A. S., Gavazzi R., Koopmans L. V. E., Marshall P. J., Bundy K., Moustakas L. A., 2009, ApJ, 705, 1099
Auger M. W., Treu T., Bolton A. S., Gavazzi R., Koopmans L. V. E., Marshall P. J., Moustakas L. A., Burles S., 2010, ApJ, 724, 511
Barnabè M., Czoske O., Koopmans L. V. E., Treu T., Bolton A. S., 2011, MNRAS, 415, 2215
Beckmann R. S. et al., 2017, MNRAS, 472, 949
Birnboim Y., Dekel A., 2003, MNRAS, 345, 349
Bolton A. S. et al., 2012, ApJ, 757, 82
Bolton A. S., Burles S., Koopmans L. V. E., Treu T., Moustakas L. A., 2006, ApJ, 638, 703
Bolton A. S., Burles S., Koopmans L. V. E., Treu T., Gavazzi R., Moustakas L. A., Wayth R., Schlegel D. J., 2008, ApJ, 682, 964
Booth C. M., Schaye J., 2009, MNRAS, 398, 53
Brownstein J. R. et al., 2012, ApJ, 744, 41
Cappellari M., 2016, ARA&A, 54, 597
Czoske O., Barnabè M., Koopmans L. V. E., Treu T., Bolton A. S., 2012, MNRAS, 419, 656
Dekel A. et al., 2009, Nature, 457, 451
Djorgovski S., Davis M., 1987, ApJ, 313, 59
Dressler A., Lynden-Bell D., Burstein D., Davies R. L., Faber S. M., Terlevich R., Wegner G., 1987, ApJ, 313, 42
Dubois Y. et al., 2014, MNRAS, 444, 1453
Dubois Y., Devriendt J., Slyz A., Teyssier R., 2010, MNRAS, 409, 985
Dubois Y., Devriendt J., Slyz A., Teyssier R., 2012, MNRAS, 420, 2662
Dubois Y., Gavazzi R., Peirani S., Silk J., 2013, MNRAS, 433, 3297
Dubois Y., Peirani S., Pichon C., Devriendt J., Gavazzi R., Welker C., Volonteri M., 2016, MNRAS, 463, 3948
Duffy A. R., Schaye J., Kay S. T., Dalla Vecchia C., Battye R. A., Booth C. M., 2010, MNRAS, 405, 2161
Dutton A. A., Treu T., 2014, MNRAS, 438, 3594
Dutton A. A., Macciò A. V., Mendel J. T., Simard L., 2013, MNRAS, 432, 2496
Dye S. et al., 2014, MNRAS, 440, 2013
Faber S. M., Dressler A., Davies R. L., Burstein D., Lynden-Bell D., 1987, in Faber S. M., ed., Nearly Normal Galaxies. From the Planck Time to the Present. Springer-Verlag, Berlin, p. 175
Ferrarese L., Merritt D., 2000, ApJ, 539, L9
Gavazzi R., Treu T., Rhodes J. D., Koopmans L. V. E., Bolton A. S., Burles S., Massey R. J., Moustakas L. A., 2007, ApJ, 667, 176
Gavazzi R., Treu T., Marshall P. J., Brault F., Ruff A., 2012, ApJ, 761, 170
Gavazzi R., Marshall P. J., Treu T., Sonnenfeld A., 2014, ApJ, 785, 144
Gültekin K. et al., 2009, ApJ, 698, 198
Häring N., Rix H.-W., 2004, ApJ, 604, L89
Hirschmann M., Naab T., Somerville R. S., Burkert A., Oser L., 2012, MNRAS, 419, 3200
Jiang G., Kochanek C. S., 2007, ApJ, 671, 1568
Jiménez-Vicente J., Mediavilla E., Kochanek C. S., Muñoz J. A., 2015, ApJ, 799, 149
Johansson P. H., Naab T., Ostriker J. P., 2012, ApJ, 754, 115
Kaviraj S. et al., 2017, MNRAS, 467, 4739
Kereš D., Katz N., Weinberg D. H., Davé R., 2005, MNRAS, 363, 2
King A., 2003, ApJ, 596, L27
Komatsu E. et al., 2011, ApJS, 192, 18
Koopmans L. V. E. et al., 2009, ApJ, 703, L51
Koopmans L. V. E., Treu T., 2003, ApJ, 583, 606
Koopmans L. V. E., Treu T., Bolton A. S., Burles S., Moustakas L. A., 2006, ApJ, 649, 599
Lackner C. N., Ostriker J. P., 2010, ApJ, 712, 88
Lackner C. N., Cen R., Ostriker J. P., Joung M. R., 2012, MNRAS, 425, 641
Lagattuta D. J. et al., 2010, ApJ, 716, 1579
Loeb A., Peebles P. J. E., 2003, ApJ, 589, 29
Magorrian J. et al., 1998, AJ, 115, 2285
Martizzi D., Teyssier R., Moore B., 2013, MNRAS, 432, 1947
Miralda-Escude J., 1995, ApJ, 438, 514
Natarajan P., Kneib J.-P., 1996, MNRAS, 283, 1031
Newman A. B., Treu T., Ellis R. S., Sand D. J., Richard J., Marshall P. J., Capak P., Miyazaki S., 2009, ApJ, 706, 1078
Newman A. B., Treu T., Ellis R. S., Sand D. J., 2013, ApJ, 765, 25
Newman A. B., Ellis R. S., Treu T., 2015, ApJ, 814, 26
Nipoti C., Treu T., Auger M. W., Bolton A. S., 2009, ApJ, 706, L86
Nipoti C., Treu T., Leauthaud A., Bundy K., Newman A. B., Auger M. W., 2012, MNRAS, 422, 1714
Ocvirk P., Pichon C., Teyssier R., 2008, MNRAS, 390, 1326
Oguri M., Rusu C. E., Falco E. E., 2014, MNRAS, 439, 2494
Omma H., Binney J., Bryan G., Slyz A., 2004, MNRAS, 348, 1105
Peirani S. et al., 2017, MNRAS, 472, 2153
Peirani S., Kay S., Silk J., 2008, A&A, 479, 123
Posacki S., Cappellari M., Treu T., Pellegrini S., Ciotti L., 2015, MNRAS, 446, 493
Power C., Navarro J. F., Jenkins A., Frenk C. S., White S. D. M., Springel V., Stadel J., Quinn T., 2003, MNRAS, 338, 14
Rees M. J., Ostriker J. P., 1977, MNRAS, 179, 541
Remus R.-S., Burkert A., Dolag K., Johansson P. H., Naab T., Oser L., Thomas J., 2013, ApJ, 766, 71
Remus R.-S., Dolag K., Naab T., Burkert A., Hirschmann M., Hoffmann T. L., Johansson P. H., 2017, MNRAS, 464, 3742
Renzini A., 2006, ARA&A, 44, 141
Ruff A. J., Gavazzi R., Marshall P. J., Treu T., Auger M. W., Brault F., 2011a, ApJ, 727, 96
Ruff A. J., Gavazzi R., Marshall P. J., Treu T., Auger M. W., Brault F., 2011b, ApJ, 727, 96
Sand D. J., Treu T., Ellis R. S., 2002, ApJ, 574, L129
Schaller M. et al., 2015, MNRAS, 452, 343
Schaye J. et al., 2015, MNRAS, 446, 521
Schechter P. L., Pooley D., Blackburne J. A., Wambsganss J., 2014, ApJ, 793, 96
Shakura N. I., Sunyaev R. A., 1973, A&A, 24, 337
Shankar F. et al., 2017, ApJ, 840, 34
Sheth R. K. et al., 2003, ApJ, 594, 225
Shu Y. et al., 2015, ApJ, 803, 71
Shu Y. et al., 2016, ApJ, 833, 264
Silk J., Rees M. J., 1998, A&A, 331, L1
Smith R. J., Lucey J. R., Conroy C., 2015, MNRAS, 449, 3441
Sonnenfeld A., Gavazzi R., Suyu S. H., Treu T., Marshall P. J., 2013a, ApJ, 777, 97

Sonnenfeld A., Treu T., Gavazzi R., Suyu S. H., Marshall P. J., Auger M. W., Nipoti C., 2013b, ApJ, 777, 98
Sonnenfeld A., Nipoti C., Treu T., 2014, ApJ, 786, 89
Sonnenfeld A., Treu T., Marshall P. J., Suyu S. H., Gavazzi R., Auger M. W., Nipoti C., 2015, ApJ, 800, 94
Sonnenfeld A., Leauthaud A., Auger M. W., Gavazzi R., Treu T., More S., Komiyama Y., 2018, MNRAS, 481, 164
Teyssier R., 2002, A&A, 385, 337
Tortora C., La Barbera F., Napolitano N. R., Romanowsky A. J., Ferreras I., de Carvalho R. R., 2014, MNRAS, 445, 115
Treu T., Koopmans L. V. E., 2002, ApJ, 575, 87
Treu T., Koopmans L. V. E., 2004, ApJ, 611, 739
Treu T., Koopmans L. V., Bolton A. S., Burles S., Moustakas L. A., 2006, ApJ, 640, 662
Treu T., Gavazzi R., Gorecki A., Marshall P. J., Koopmans L. V. E., Bolton A. S., Moustakas L. A., Burles S., 2009, ApJ, 690, 670
Treu T., Auger M. W., Koopmans L. V. E., Gavazzi R., Marshall P. J., Bolton A. S., 2010, ApJ, 709, 1195
Tu H. et al., 2009, A&A, 501, 475
van de Voort F., Schaye J., Booth C. M., Haas M. R., Dalla Vecchia C., 2011, MNRAS, 414, 2458
Vogelsberger M. et al., 2014, MNRAS, 444, 1518
Volonteri M., Dubois Y., Pichon C., Devriendt J., 2016, MNRAS, 460, 2979
Welker C., Dubois Y., Devriendt J., Pichon C., Kaviraj S., Peirani S., 2017, MNRAS, 465, 1241
White S. D. M., Frenk C. S., 1991, ApJ, 379, 52
White S. D. M., Rees M. J., 1978, MNRAS, 183, 341
Wyithe J. S. B., Loeb A., 2003, ApJ, 595, 614
Xu D., Springel V., Sluse D., Schneider P., Sonnenfeld A., Nelson D., Vogelsberger M., Hernquist L., 2017, MNRAS, 469, 1824

APPENDIX A: RESOLUTION TESTS

In order to investigate the effects of resolution on our results, we compare our fiducial simulations (i.e. $H_{\rm AGN}$) with lower resolution versions (i.e. 512^3 and 256^3 DM particles with initial uniform grid refined down to $\Delta x = 2$ and $\Delta x = 4$ proper kpc, respectively). To have a clear diagnostic, we focus on the average density profiles of DM haloes at two epochs, $z = 1$ and $z = 0.3$. In order to match DM haloes and galaxies between the three simulations, we use the same scheme developed in Peirani et al. (2017) and summarized in Section 2.2. The main difference here is that one given DM particle of any of the two lower resolution simulations is associated to eight particles in the subsequent higher resolution version (i.e. between HORIZON-AGN and HORIZON-AGN -512^3 or between HORIZON-AGN -512^3 and HORIZON-AGN -256^3). However, it is still possible to know the composition of each DM halo and the fraction of common particles between two objects of different simulation versions. If this fraction is greater than 50 per cent, we consider that these DM haloes are twin.

In the following, we select galaxy samples of a given mass range in the $H_{\rm AGN}$ simulation and at $z = 1$ or $z = 0.3$. We then identified their matching galaxies in HORIZON-AGN -512^3 and HORIZON-AGN -256^3 when possible. Finally, we identify their respective host halo to produce samples of DM haloes between the three simulations. Only DM haloes which can be matched between the three simulations are kept.

Fig. A1 compares the mean DM density profile for DM haloes hosting galaxies with a mass M_* defined by $2 \times 10^{11}\,{\rm M}_\odot \geq M_* \geq 10^{11}\,{\rm M}_\odot$ at $z = 1$. In this case, we have considered 474 matched objects. As we can see, resolution effects cause the density to be overestimated in the inner parts of DM haloes. Moreover, as shown in Fig. A2, we get the same trends at $z = 0.3$ using a similar galaxy mass interval or considering more massive galaxies ($M_* \geq 5 \times 10^{11}\,{\rm M}_\odot$). We have considered here samples of 846 and 89 DM haloes, respectively, to derive the mean density profiles.

Power et al. (2003) recommend to use lower limit values of 5, 10, and 20 kpc, respectively, for $H_{\rm AGN}$, $H_{\rm AGN}$ (512^3), and $H_{\rm AGN}$ (256^3) and for our the studied halo/galaxy mass range. Although their analysis concerns pure DM simulations only, Figs A1 and A2 strongly suggest that lower limits defined by Power et al. (2003) give a clear and satisfactory indication of where the density profiles should converge.

Finally, we can also investigate the effect of resolution in the prediction of observable quantities relevant to this work such as the effective radius $R_{\rm e}$ and the total density slope $\gamma'_{\rm tot}$. We therefore generate similar figures than Figs 1–4 with adding results derived from HORIZON-AGN -512^3 and HORIZON-AGN -256^3. One can see in Fig. A3 that the trends are quite similar between results from the three simulations, especially those relative to the variations of $\gamma'_{\rm tot}$ (upper right panel and lower ones). However, there are some slight differences induced by the baryon component treatment. Indeed, higher resolutions imply in general higher gas densities especially in the central part of haloes which can lead to more gas cooling. Therefore, the galaxies produced in the higher resolution simulations tend to be slightly more massive and more concentrated as the star formation tend to be more efficient in the inner regions. In this case, such galaxies have on the average lower $R_{\rm e}$ values as suggested by the upper left panel of Fig. A3. However, values of $R_{\rm e}$ from the considered stellar mass range are quite close between the different simulations and this seems not to particularly affect the estimation of γ' in the interval $[R_{\rm e}/2 - R_{\rm e}]$.

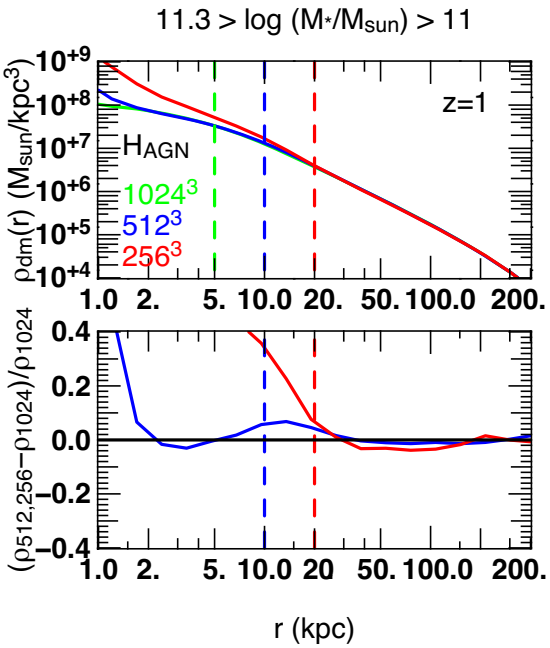

Figure A1. Comparison of the mean DM density profiles (and residual) of haloes hosting a galaxy with a mass of $2 \times 10^{11} \geq M_* \geq 10^{11}\,{\rm M}_\odot$ at $z = 1$, derived from the $H_{\rm AGN}$ simulation (green line) and lower resolution versions, HORIZON-AGN -512^3 (blue line) and HORIZON-AGN -256^3 (red line). The dashed vertical lines (with same colour code) correspond to recommended lower limit values suggested by Power et al. (2003) for each simulation which give satisfactory indication of where the density profiles should converge.

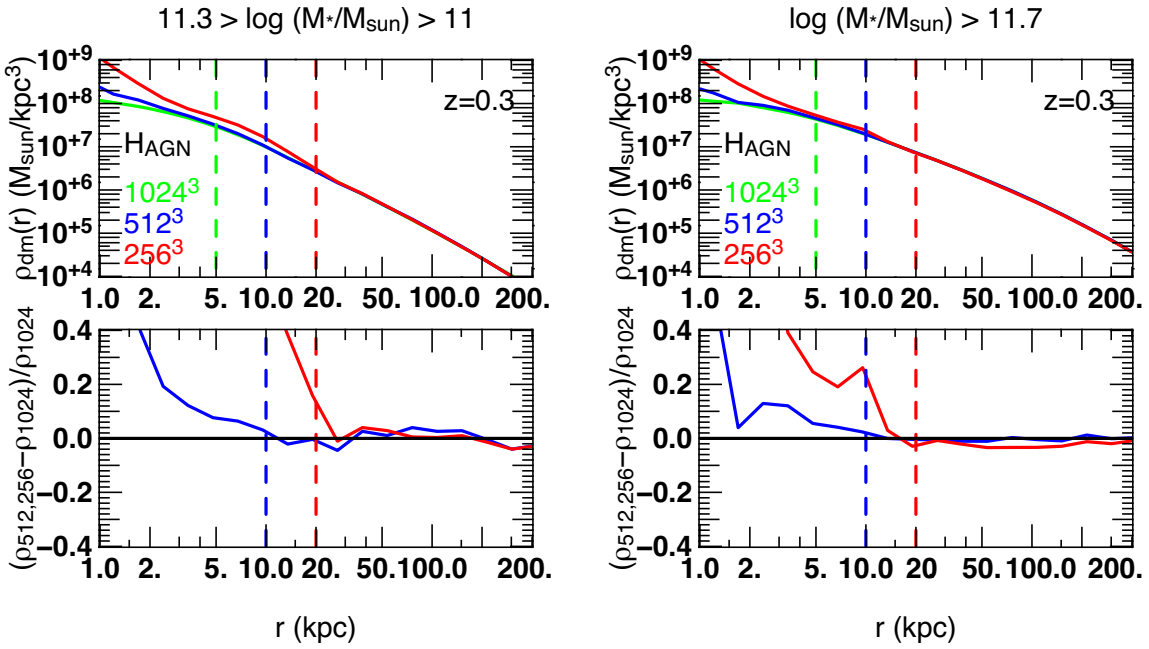

Figure A2. As in Fig. A1 but for DM haloes hosting a galaxy with a mass of $2 \times 10^{11}\,M_{\odot} \geq M_{*} \geq 10^{11}\,M_{\odot}$ (left-hand panel) or $M_{*} \geq 5 \times 10^{11}\,M_{\odot}$ (right-hand panel) at $z = 0.3$. Same trends are obtained.

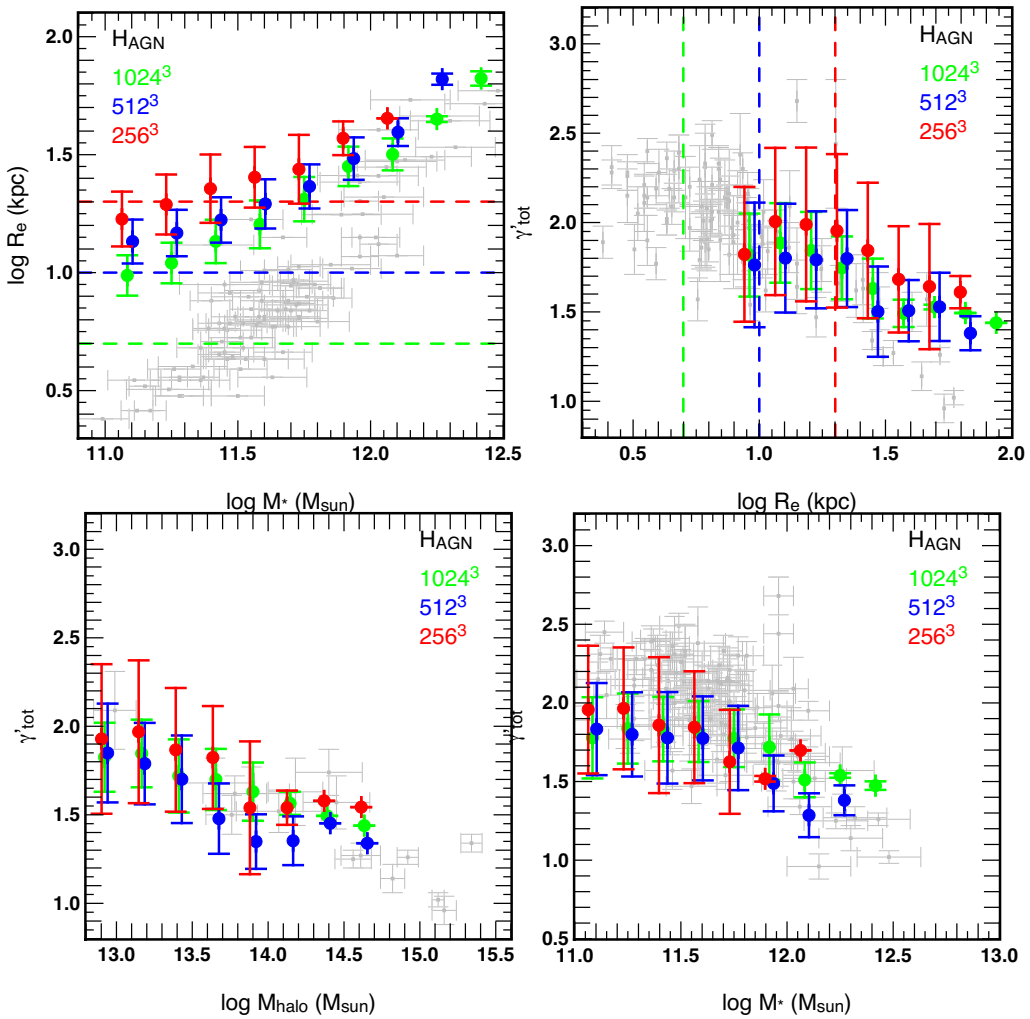

Figure A3. The variations of the effective radius R_e with respect to the stellar mass M_* (upper left panel) and the variations of the mass-weighted total density slopes γ'_{tot} with respect to the effective radius R_e (upper right panel), to the DM halo masses M_{halo} (lower left panel) and to the stellar masses M_* (lower right panel). Green colour refers to our fiducial H_{AGN} simulation while blue and red colours correspond to results from matching galaxies from HORIZON-AGN -512^3 and HORIZON-AGN -256^3, respectively. The dashed lines (with same colour code) correspond to recommended lower limit values suggested by Power et al. (2003) for each simulation. Grey data are observational data used in Figs 1–4. In spite of slight differences, same trends are obtained from the three runs in the considered galaxy mass range.

This paper has been typeset from a TEX/LATEX file prepared by the author.